nature communications

Article

https://doi.org/10.1038/s41467-025-62112-2

Unconventional low temperature decomposition of a saturated hydrocarbon over atomically-dispersed titanium-aluminum-boron catalyst

Received: 19 June 2024

Accepted: 10 July 2025

Published online: 23 July 2025

Check for updates

Souvick Biswas[1,7], Jack Cokas[2,7], Winston Gee[2], Dababrata Paul[1], Nureshan Dias[3], Harry W. T. Morgan[2], Matthew T. Finn[4], Bethany M. Hudak[5], Perrin M. Godbold[6], Christopher A. Klug[4], Albert Epshteyn[4] ✉, Anastassia N. Alexandrova[2] ✉, Musahid Ahmed[3] ✉ & Ralf I. Kaiser[1] ✉

Sonochemically-synthesized atomically-dispersed titanium-aluminum-boron nanopowder (TiAlB NP) exhibits a remarkable low-temperature catalytic activation of aliphatic C-H bonds at 750 K followed by C-C bond activation thus emerging as a potent low-cost alternative to expensive platinum group metals. Here, the model saturated hydrocarbon, *exo*-tetrahydrodicyclopentadiene ($C_{10}H_{16}$), undergoes catalytic decomposition on TiAlB NPs in a chemical microreactor to produce 1,3-cyclopentadiene (c-C_5H_6), cyclopentene (c-C_5H_8), and molecular hydrogen (H_2) as detected in situ via isomer-selective, single-photon ionization time-of-flight mass spectrometry. Extensive electronic structure theory calculations on model clusters of the catalyst decode a unique synergy among the atomic constituents of the catalyst and chemical bonding in this stepwise, retro Diels Alder reaction: Ti, although insensitive to C-H activation in its metallic state, initiates the catalysis via chemisorption of the hydrocarbon, adjacent B centers readily abstract hydrogen atoms and store them during the catalytic cycle, while Al stabilizes the catalyst structure yet providing space for critical docking sites for the departing hydrocarbons.

The very first discovery of the fundamental concept of heterogeneous catalysis by Johann Wolfgang Döbereiner in 1822 was demonstrated utilizing platinum (Pt) powder to catalyze the ignition of molecular hydrogen[1]. During the last two centuries, Pt has emerged as one of the most efficient transition metal catalysts due to its superior catalytic performance for oxidation[2–4], hydrogenation[5,6], and industrial hydrocarbon cracking processes[7]. Saturated hydrocarbons in particular such as propane (C_3H_8) and *exo*-tetrahydrodicyclopentadiene (*exo*-$C_{10}H_{16}$) are predominant sources of fuel for energy production[8]. They further represent vital precursors for key chemicals on the industrial scale, e.g., alkenes (propylene (C_3H_6), ethylene (C_2H_4))[9] and their corresponding polymers (polypropylene, polyethylene)[10] along with aromatics (benzene)[11] as feedstock of numerous end-use products like pharmaceuticals and detergents.

The key prerequisite of these chemical transformations involves the reduction of the barrier for the initial C–H bond cleavage with

[1]Department of Chemistry, University of Hawaii at Manoa, Honolulu, Hawaii, USA. [2]Department of Chemistry and Biochemistry, University of California, Los Angeles, Los Angeles, CA, USA. [3]Chemical Sciences Division, Lawrence Berkeley National Laboratory, Berkeley, CA, USA. [4]Chemistry Division, U.S. Naval Research Laboratory, Washington, DC, USA. [5]Materials Science and Technology Division, U.S. Naval Research Laboratory, Washington, DC, USA. [6]NRC Postdoctoral Associate, Chemistry Division, U.S. Naval Research Laboratory, Washington, DC, USA. [7]These authors contributed equally: Souvick Biswas, Jack Cokas. ✉e-mail: albert.epshteyn@nrl.navy.mil; ana@chem.ucla.edu; mahmed@lbl.gov; ralfk@hawaii.edu

typical carbon-hydrogen bond dissociation energies of at least 400 kJ mol^{-1}[12]. Homogeneous Pt-based catalysts such as *trans*-$PtCl_2(NO_2)(H_2O)^-$ and *cis*-$PtCl_2(NH_3)_2$ facilitate a catalytic activation and hence facile homolytic rupture of stable (sp^3) C–H bonds[13,14] by reducing this barrier to only 39 kJ mol^{-1} and 29 kJ mol^{-1}, respectively[1], thus achieving optimum energy efficiency in these processes[15]. From the mechanistic point of view, the reaction sequence begins with the saturated hydrocarbon undergoing physisorption from the gas-phase onto the catalyst surface with the subsequent carbon-hydrogen bond dissociation (a notoriously unfavorable step at high temperatures). The activated or dissociative chemisorption on the catalyst surface emerged as the rate-limiting step of the overall reaction[16]. Owing to their strong affinity towards (sp^3) C–H bonds, noble metals, such as Pt, despite the high cost and low abundance, have remained the most widely used catalysts for hydrocarbon dehydrogenation[17–20]. Metal additives such as tin (Sn), gallium (Ga), cobalt (Co), and copper (Cu), which are catalytically inactive on their own, do enhance catalyst selectivity and increase its lifetime by preventing coke formation[21–30].

However, Pt's scarcity in nature[31] and high cost[32] are strong motivators for the development of next generation heterogeneous cracking catalysts that preserve the high activity of Pt, while simultaneously focusing on economically friendly more abundant elements that preserve the chemical selectivity of the catalyst. Titanium (Ti) has been suggested as such an alternative, given that it activates even the hydrogen-hydrogen bond of molecular hydrogen by reducing the activation energy from 436 kJ mol^{-1} in the gas phase to 142 kJ mol^{-1} at 873 K and 750 Torr of hydrogen, thus Ti has been conceived to be a hydrogen storage material[33–35]. Additionally, Ti possesses the advantages of a significant natural abundance and low cost for refinement. The hydrogen adsorption capacity of Ti can be enhanced in the presence of affordable light elements like aluminum (Al) and boron (B) which are prone to hydride formation[36–39]. However, unlike Pt and d^8-metals (nickel (Ni), palladium (Pd)), metallic Ti in its elemental state (d^2-system) alone is unable to exert any significant C-H bond activation effect, rather it is shown to have a repelling effect on the saturated hydrocarbons such as methane[40,41].

A unique approach to the synthesis of multi-metal nanopowders has been developed, where using a sonochemically-mediated slurry technique, complex metal hydride precursors are generated in situ and are decomposed to produce amorphous nanopowders[42–45]. Materials with multiple compositions have been prepared via this technique, such as Ti-Al[42], Ti-B[43], and Ti-Al-B[44,45]. Most importantly, these materials are produced and collected at low temperature in a controlled reaction environment, resulting in a localized atomic structure with a unique atomic arrangement not attainable by other synthetic techniques[43–45].

To untangle the catalysis at the molecular level by these mixed-metal nanopowders for saturated hydrocarbons it is imperative to identify the nascent products/intermediates in situ. Although popular off-line and ex-situ detection tools such as gas chromatography (GC) and GC-coupled mass spectrometry (GC–MS) can identify closed-shell products, short-lived reaction intermediates cannot be probed by these methods. These reactive intermediates (e.g., radicals) formed in the initial stages of the catalytic conversion are not only crucial to decipher the underlying chemistry but also control the overall efficiency and performance of the respective catalysts. Additionally, a comprehensive inventory of the temperature-dependent products and intermediates is essential for understanding the thermocatalytic properties of these nanopowders as a function of temperature. Therefore, in the present study, an isomer-selective in situ diagnostics approach utilizing photoionization to probe the reaction products in a molecular beam has been adopted at temperatures ranging from 300 K to 1050 K. This method utilizes the power of soft photoionization with single photon synchrotron vacuum ultraviolet (VUV) light followed by a mass spectroscopic analysis of the ions in a reflectron time-of-flight mass spectrometer (Re-TOF-MS). For a particular mass-to-charge ratio (m/z), the ion counts as a function of photon energy scan yields in corresponding photoionization efficiency (PIE) curve, which is a unique characteristic for a particular species—identifies the threshold ionization energy and also capable of excellent discrimination of isomers.

Here, by combining the abovementioned molecular beam experiments with electronic structure calculations, we reveal a facile C-H bond activation and efficient heterogeneous catalytic cycle of a low-temperature decomposition of *exo*-tetrahydrodicyclopentadiene (*exo*-$C_{10}H_{16}$) over sonochemically-synthesized titanium-aluminum-boron nanopowder (TiAlB NP) in a chemical microreactor[46–48] (Fig. 1). Compared to the gas-phase, the threshold temperature of the decomposition of *exo*-$C_{10}H_{16}$ is reduced dramatically by 450 K from 1200 K to only 750 K in the presence of TiAlB NP selectively generating 1,3-cyclopentadiene (c-C_5H_6) and cyclopentene (c-C_5H_8)/1,3-

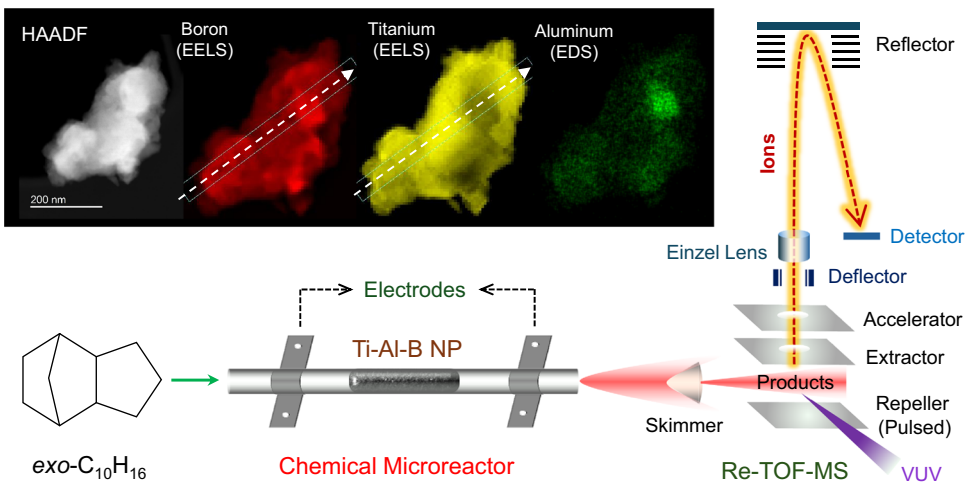

Fig. 1 | Schematic of the catalytic microreactor-coupled molecular beam machine along with the electron microscopy image and mapping of the constient elements for TiAlB NP. Decomposition of helium-seeded *exo*-tetrahydrodicyclopentadiene (*exo*-$C_{10}H_{16}$) in a high-temperature chemical microreactor over titanium-aluminum-boron reactive mixed metal nanopowder (TiAlB NP) where the products are photoionized exploiting synchroton vacuum ultraviolet (VUV) beam followed by detection in a reflectron time-of-flight mass spectrometer (Re-TOF-MS). The high-angle annular dark-field (HAADF) scanning transmission electron microscopy (STEM) image of TiAlB NP showing the uniform distribution of the metals with minimal phase segregation as probed by complementary electron energy loss spectroscopy (EELS) and energy-dispersive X-ray spectroscopy (EDS) are depicted in the inset.

https://doi.org/10.1038/s41467-025-62112-2

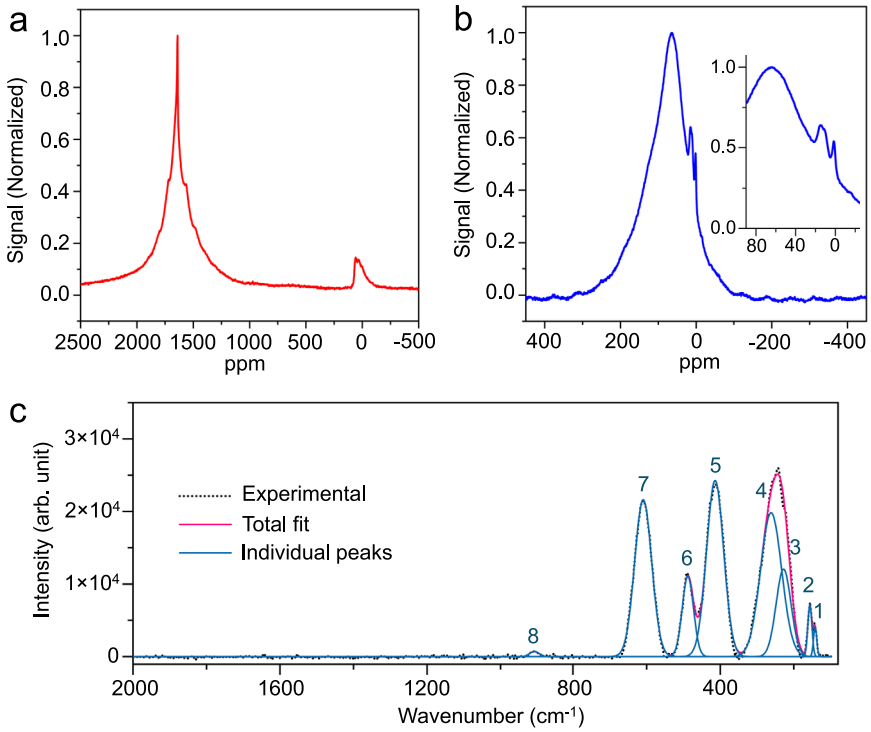

Fig. 2 | Solid-state NMR and Raman spectra of TiAlB NP. a ^{27}Al (*red* trace, top left panel) and **b** ^{11}B (*blue* trace, top right panel) magic angle spinning (MAS) NMR spectra of titanium-aluminum-boron nanopowder (TiAlB NP). **c** Deconvoluted Raman spectra of TiAlB NP (bottom panel), where the experimental spectrum is depicted as *black* dotted line and individual fitted peaks and total fits are presented in *ocean blue* and *pink* solid lines, respectively.

pentadiene (C_5H_8). Complementary electronic structure calculations are in accord with our experimental findings with multiple TiAlB clusters sampled as model systems representing multiple possible complex catalyst surface atomic arrangements. Overall, the complex heterogeneous catalysis reaction sequence involves a cycle of molecular adsorption, reaction, isomerization, and desorption, which commences with a facile Ti/B-mediated carbon-hydrogen bond rupture at 750 K having a barrier of only 30 kJ mol^{-1}. This process activates the C-H bond (397 kJ mol^{-1}) in *exo*-$C_{10}H_{16}$[49], thus rivaling the catalytic activity of Pt in the pyrolysis and cracking of hydrocarbons. The comprehensive molecular level understanding provided here is essential in deciphering the specific roles of distinct metals in this new class of heterogeneous hybrid catalysts applicable in, e.g., the thermal decomposition and isomer-selective cracking of hydrocarbons. For this class of heterogeneous C−H activation processes, thermally fragile organometallic complexes have not been found useful. The concern of thermal instability of the organic ligands therein is shown here to be overcome by synthesizing atomically dispersed TiAlB NP (Supplementary Fig. 1), where Ti acts as a central docking and activation site due to its large atomic size compared to B and Al along with its potential to form a deeply bound (−117 kJ mol^{-1}) van-der-Waals complex with the hydrocarbon, while B and Al assist the hydrogen transfer process thus providing an atomistic view of efficient catalysis exploiting readily available elements.

Results and discussion

Characterization of titanium-aluminum-boron nanopowder

The amorphous titanium-aluminum-boron nanopowder (TiAlB NP) shows fairly uniform distribution of the constituent elements with minimal phase segregation (Fig. 1) as revealed by the high-angle annular dark-field scanning transmission electron microscopy (STEM) coupled with complementary electron energy loss spectroscopy and energy-dispersive X-ray spectroscopy. The ^{27}Al magic angle spinning (MAS) NMR spectrum (Fig. 2a) of the nanopowder contains an intense peak near 1642 ppm associated with the elemental [Al(0)] state, along with a smaller asymmetric peak near 75 ppm corresponding to aluminate (-OAl) with a range of coordinations[50,51]. In the ^{11}B MAS NMR spectrum, the dominant feature is a relatively broad peak centered near 65 ppm, which exactly resembles the 3-fold coordinated boron center of anionic B_6 moiety[52]. The observed chemical shift is governed by Pauli paramagnetism of the conducting electrons on the boron nuclei, which in turn depends on the chemical nature (e.g., electropositivity, valence orbital, etc.) of the metal counterpart. Hence, the presence of Ti and Al results into a slight deviation for the observed chemical shift from the reported peak of 84 ppm for KB_6. Similar chemical shift (66 ppm) for a softer metal-boron interaction in the form of Au—B linkage $[(B_2P_2)Au]^-$ (B_2P_2: phosphine substituted 9,10-diboraanthracene ligand) was also recorded earlier[53], indicating a higher degree of covalency in the TiAlB nanopowder. On the other hand, the width of the band (Fig. 2b) plausibly originated due to residual dipolar interaction with electron spins (such as metal-boron or metal-boron-metal linkages) or with other ^{11}B nuclei (homonuclear) despite MAS. Additional small peaks in the range of 0-20 ppm (Fig. 2b, inset) represent tetrahedral coordination of boron similar to those observed for $Al_{6-x}B_xO_9$ type of compounds[54].

Micro-Raman spectrum of the material (Fig. 2c, Supplementary Table 1) reveals crucial information about the interatomic linkages, such as Ti−Al−B bending [peak 2 (157 cm^{-1}) and peak 4 (257 cm^{-1})], Ti−Al stretching [peak 3 (226 cm^{-1})], Ti−B stretching [peak 5 (414 cm^{-1})], Al−B stretching [peak 6 (489 cm^{-1})] and Ti−B−Al bending [peak 7 (609 cm^{-1})][55–57]. In addition, traces of phase-segregated TiB_2 (phonon mode, peak 8) and TiO_2 (O−Ti−O bending, peak 1) can also be identified from the spectrum[58]. Corroborating the Raman spectra, X-ray photoelectron spectroscopy results depict the trace presence of multiple oxidation states of Ti along with traces of surface oxides of other constituents (Supplementary Discussion 1). These surface oxides have likely been generated via spontaneous oxidation during the unavoidable exposure to air while performing the characterizations.

https://doi.org/10.1038/s41467-025-62112-2

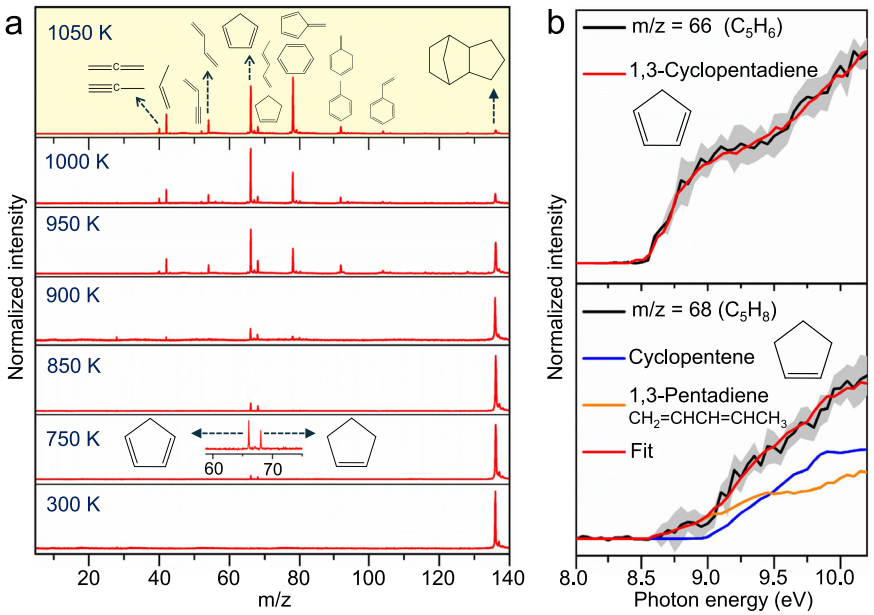

Fig. 3 | Mass spectra with increasing temperature and initial catalytic decomposition products. a Mass spectra recorded during the decomposition of helium-seeded *exo*-tetrahydrodicyclopentadiene (*exo*-$C_{10}H_{16}$) over titanium-aluminum-boron nanopowder (TiAlB NP) in a high-temperature chemical microreactor at a photon energy of 10.0 eV in the 300 K to 1050 K range (left panel). The major products identified from photoionization efficiency (PIE) curves are depicted at the initial (750 K) and complete decomposition (1050 K) temperatures. **b** Experimental PIE curves (*black* traces) of the initial decomposition products at 750 K (right panel). The experimental errors (*gray* shaded area) originate from the accuracy of the photocurrent measured by the photodiode and a 1σ error of the PIE curves averaged over the individual scans. The experimental PIE curve for m/z = 66 (top right panel) is fitted with the reference PIE curve of 1,3-cyclopentadiene (*red* trace). The multiple isomers for m/z = 68 (bottom right panel) are detected by matching with a linear combination of two reference PIE curves [cyclopentene (*blue* trace) and 1,3-pentadiene (*orange* trace)] of different structural isomers; the overall fit is depicted in a *red* trace.

However, Raman spectral data ensures that the Ti-Al-B framework is predominant in the material compared to the surface oxides existing as impurity.

Identification of decomposition products and intermediates

The catalytic thermal decomposition process of the hydrocarbon *exo*-$C_{10}H_{16}$ through the chemical microreactor packed with TiAlB NP has been traced by recording mass spectra (Fig. 3a) upon ionizing the molecular beam containing the nascent products at a photon energy of 10.0 eV (Supplementary Fig. 5). These mass spectra are recorded systematically at definite temperature intervals. At 300 K, only the parent mass peak at m/z = 136 ($C_{10}H_{16}^+$) followed by the weak features of its ^{13}C counterpart at m/z = 137 ($^{13}CC_9H_{16}^+$) are noted. The thermal decomposition of *exo*-$C_{10}H_{16}$ in presence of TiAlB NP is initiated only at 750 K with the first appearance of the weak product peaks at m/z = 66 and 68, whereas the decomposition onset temperature for uncatalyzed reaction has been found to be 1200 K under otherwise identical experimental conditions[49]. Exploiting a detailed analysis of distinct *isomer-selective* PIE curves of individual mass-to-charge (m/z) peaks, a comprehensive knowledge of the products and intermediates formed in the molecular beam is acquired. These PIE curves are unique to a particular species and enable an explicit identification of the nascent products. Figure 3b reveals the initially decomposed products of *exo*-$C_{10}H_{16}$ in presence of the catalyst to be 1,3-cyclopentadiene (c-C_5H_6, m/z = 66), cyclopentene (c-C_5H_8, m/z = 68), and its open-chain isomer 1,3-pentadiene (C_5H_8, m/z = 68). Considering *exo*-$C_{10}H_{16}$ - a fused, strained dimeric unit of cyclic five-membered ring, the yield of above-mentioned cyclic species indicates facile ring-opening via a strong C-H activation followed by successive C-C bond cleavages. Cyclopentene (c-C_5H_8) can isomerize to 1,3-pentadiene (C_5H_8) in the gas phase at the given temperature[49].

Mass spectra recorded at a photon energy of 15.4 eV (Supplementary Fig. 6) additionally detects molecular hydrogen (H_2, m/z = 2) indicating a catalytic dehydrogenation reaction in operation. Note that the rise in temperature results in increased chemical complexity of the decomposition; in other words, the number of mass peaks increases with a simultaneous decay of the parent hydrocarbon ion count at m/z = 136, which nearly disappears at 1050 K. However, molecular mass growth processes beyond the parent peaks (m/z = 136, 137) are absent suggesting the exclusive detection of the primary products in the experimental setup.

The PIE curves at distinct temperatures (Supplementary Figs. 7, 8, 9) above 750 K reveal that the diversity in the products enhances with an increase in temperature. At the maximum experimental temperature (1050 K) representing the full decomposition of *exo*-$C_{10}H_{16}$, distinct classes of species are detected (Supplementary Table 2) - including open-chain, cyclic and aromatic closed-shell hydrocarbons and radicals[59]. Traces of methane (CH_4, m/z = 16), the simplest hydrocarbon have also been identified from the corresponding mass spectra at 15.4 eV (Supplementary Fig. 6) for this temperature. However, a comparison of these products with those formed in the gas phase pyrolysis of *exo*-$C_{10}H_{16}$ indicates (Supplementary Table 2) a more uniform product formation in the former. It is also important to note that in the repeated experiments (Experimental Methods) with the catalyst loading via stepwise heating-cooling-heating procedure at a specific temperature, no observable alteration in the mass-spectra was detected which further ensures unaltered chemical activity and excellent life-cycle of the catalyst. The Raman spectrum of the recovered nanopowder after the catalytic cycle also confirms no significant structural changes via the acquired spectral features except minimal graphitic deposition in the reactor tube (Supplementary Fig. 10).

Decomposition profile

To quantify the progress of decomposition of the *exo*-$C_{10}H_{16}$ with respect to temperature and assess the catalytic effects of TiAlB NP, the decomposition ratio curves as a function of temperature with and

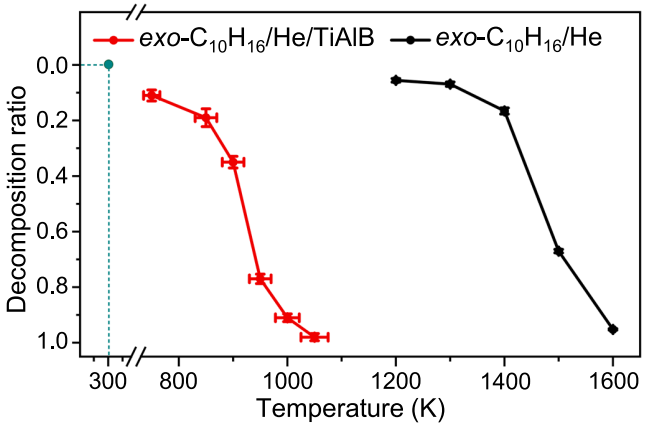

Fig. 4 | Catalytic effects revealed in the temperature-dependent decomposition ratio curve. Decomposition ratios of *exo*-tetrahydrodicyclopentadiene (*exo*-$C_{10}H_{16}$) passing through a high-temperature chemical microreactor with (*red* trace) and without (*black* trace) titanium-aluminum-boron nanopowder (TiAlB NP). Error bars of the *y*-axis originate from experimental uncertainties (2σ) of the m/z = 136 peak intensities evaluated by averaging the mass spectra, while errors of the *x*-axis are associated with the accuracy of the measured temperature. The *green* circle represents undecomposed hydrocarbon at 300 K.

without the catalyst loading are shown in Fig. 4. The decomposition ratio is defined as the ratio of the decomposed hydrocarbon to the total amount, where zero indicates no reaction, i.e., the undecomposed state (represented by the green circle in Fig. 4) and the full consumption of the hydrocarbon is represented as unity. Experimentally, the magnitude of the ratio at a particular temperature is evaluated by probing the fractions of normalized parent mass peak intensities at m/z = 136 with respect to that observed at 300 K. From the plot, it is evident that in presence of TiAlB NP, the decomposition of *exo*-$C_{10}H_{16}$ (red trace) is initiated at a significantly lower temperature of 750 K, which is 450 K below the onset temperature of decomposition reaction in the absence of the catalyst (black trace). The general pattern of both the decomposition curves appears to be similar; however, the full decomposition of *exo*-$C_{10}H_{16}$ has been noted to occur at only 1050 K in presence of TiAlB NP while the decomposition in absence of the catalyst doesn't even initiate until 1200 K and complete decomposition occurs at 1600 K. This stark difference in the decomposition ratio curves demonstrates strong catalytic effects of TiAlB NP throughout the entire operational temperature range.

The enhancement of catalytic decay of *exo*-$C_{10}H_{16}$ with respect to the rising temperature is complemented with the simultaneous increase in the product abundances which are probed as a function of temperature-dependent mass peak intensities (Supplementary Fig. 11). The trend depicts that the yield of primary product 1,3-cyclopentadiene (c-C_5H_6, m/z = 66) continues to increase but with a diminished rate in the high temperature range, while that of cyclopentene and 1,3-pentadiene (C_5H_8, m/z = 68) reach their maxima at 900 K followed by a slow decay. On the contrary, other products including short chain hydrocarbons and cyclic 6- and 9-carbon species grow significantly above 950 K, which are likely to be generated from the C5 primary products serving as the precursors.

Product branching ratios

The individual branching ratios (Supplementary Discussion 2) at four distinct temperatures (Supplementary Fig. 12) provide a quantified overview of the mole fractions (concentration) of products[46]. The initial decomposition products 1,3-cyclopentadiene (c-C_5H_6, m/z = 66) cyclopentene and 1,3-pentadiene (C_5H_8, m/z = 68) constitute the branching ratios of 44.2 ± 2.8, 35.4 ± 2.9 and 16.6 ± 2.1 %, respectively, along with 3.8 ± 1.6 % of molecular hydrogen (H_2). The C_5H_6 and total C_5H_8 species are generated in almost equal yields. 1,3-Cyclopentadiene (c-C_5H_6) continues to be the major product until 950 K (28.2 ± 3.4%), while C_5H_8 isomers tend to decline remarkably with the rise in temperature and the open-chain isomer dominates over the cyclic counterpart. It is also notable that the larger aromatic species as well as the smaller open-chain hydrocarbons are generated in greater amounts at the higher temperatures (Supplementary Fig. 12). At 1050 K, the 6-carbon aromatic species, benzene (C_6H_6) appears to be the most contributing product (27.1 ± 2.8%). The minimal detection of the open-shell species in the molecular beam such as cyclopentadienyl (C_5H_5) and phenyl (C_6H_5) radicals as compared to the uncatalyzed thermal reaction of *exo*-$C_{10}H_{16}$ signifies (Supplementary Table 4) an effective H-atom abstraction by the radicals leading to the formation of corresponding closed-shell hydrocarbons, which is in accord with the reduced yield of molecular hydrogen (H_2) - from 3.8 ± 1.6 % at 750 K to 1.5 ± 0.2 % at 1,050 K.

TiAlB model cluster

Having established experimentally that the TiAlB NPs facilitate a low-temperature decomposition of *exo*-$C_{10}H_{16}$, we explored the roles of model TiAlB clusters to decipher the mechanistic paths for the catalytic activity of TiAlB NPs, especially to untangle the specific roles of the constituents. Material characterization attempts reveal the predominant presence of elemental state of the constituents with mutual heteroatomic interactions, while STEM imaging suggests extensive spatial atomic dispersion. Raman spectroscopy data significantly outlines the interatomic linkages that could aid the prediction of model catalyst structure. Moreover, since the individual elements are incapable of efficient C-H activation, it must be the collective interatomic interactions (e.g., Ti-B, Al-B and Ti-Al) that promote the low temperature catalysis. On the other hand, the reactivity of trace metal oxides can be ruled out as no oxygenated species were identified in the resulting molecular beam (Fig. 1)[46,60]. Therefore, $TiAl_2B_6$ clusters—the chemically simplest cluster of the correct stoichiometry[61] - are theoretically modeled using a stochastic structure search. Note that no alloy of this composition exists to enable a model in the form of facetted nanoparticles, and thus the particles are expected to be closely represented by a cluster of the matching stoichiometry. Specifically, 700 initial structures were generated while ensuring that the interatomic distances fall within normal distribution from typical bond length, and the cluster stays intact. Those were optimized to the nearest local minimum, confirmed with vibrational frequency calculations. From a chemistry viewpoint, the initial decomposition temperature of 750 K has been set as the reaction temperature, since the primary heterogeneous catalysis could be best understood when secondary reaction channels such as unimolecular gas phase decomposition, extensive fragmentations, and isomerization are excluded. Among many possible structures, the lowest energy isomers of the derived $TiAl_2B_6$ cluster representing over 99.6% of the population at 750K, as calculated via Boltzmann statistics, are depicted in Fig. 5. Isomers (1), (2), (3), (5), and (7) each have one enantiomer which are not depicted but they are included in the Boltzmann statistics calculation.

The cluster framework of $TiAlB_6$ moiety reveals an asymmetric hexagonal bipyramidal topology which is preserved with no notable differences in different isomers (1) to (6). The key difference between the isomers arises due to the position of the exterior Al atom with the location of Al further away from the Ti center causing thermodynamic destabilization as a general trend (Supporting Discussion 3).

Considering the chemical bonding, pure boron clusters depict covalent 2c-2e σ-bonds along the periphery while delocalization of both the σ- and π-type bonding spans the entire cluster[62,63]. The π-system being similar to benzene can coordinate with Ti (d-block metals). From the natural population analysis (NPA) of charges on individual atoms (Fig. 6), a slight localization of electron density can be noted in the anionic B_6 moiety, which supports the observation in ^{11}B

https://doi.org/10.1038/s41467-025-62112-2

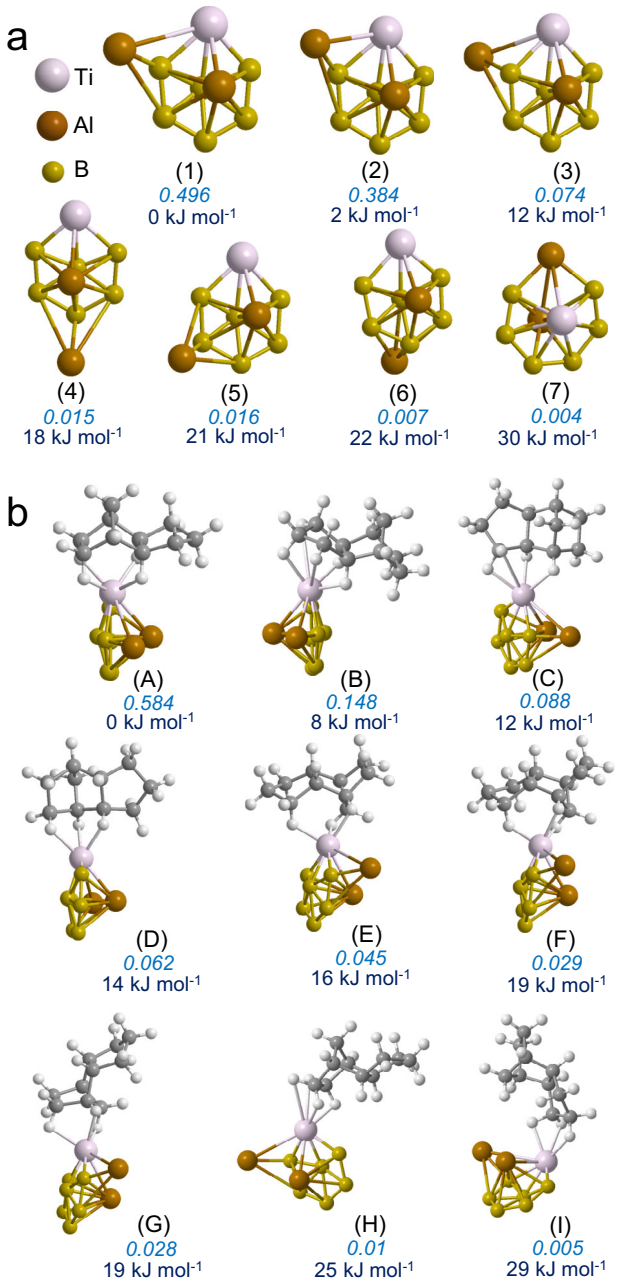

Fig. 5 | Model TiAlB clusters and the binding complexes of its global minimum with *exo*-$C_{10}H_{16}$. **a** Structures of $TiAl_2B_6$ clusters (1-7) with the corresponding Boltzmann population at 750 K (*sky blue*) and relative energies (*dark blue*) with respect to the global minimum structure (1). Except structures (4) and (6), all of the modeled clusters possess enantiomers. **b** Different binding modes (A–I) of *exo*-$C_{10}H_{16}$ with the most stable $TiAl_2B_6$ cluster (1). Below the individual complexes, their corresponding Boltzmann population at 750 K (*sky blue*) and relative energies (*dark blue*) with respect to the global minimum structure (A) are mentioned.

MAS-NMR spectrum. As discussed earlier, the NMR data reveal a 3-fold coordination of B—typical for the chemistry of boron clusters is also seen in our cluster model. The experimentally detected higher coordination number of B can be linked to the central B atom in our cluster model. On the flip side, fractional positive charges on Ti and Al atoms indicate an electrostatic interaction via charge transfer to B counterparts, as compared to extensive covalency predicted in pure B clusters. This can be corroborated to the proximity and chemical effects of the more electronegative element B in the nanopowder towards the metals in their elemental states (with little alterations) as detected experimentally. Additionally, the model cluster also deciphers the presence of interatomic linkages (e.g., Ti-B, Al-B, etc.) assigned Raman spectroscopically. However, the correlation of computed and experimental charges is only qualitative, an exact comparison between them is deemed to be overstated.

In the global minimum (1) and for the first two local minima (2,3), the exterior Al atom remains close to the Ti center, but in the third, fourth, and fifth local minima (4-6), the Al atom is far from the Ti center. At the sixth local minimum (7), the asymmetric hexagonal bipyramidal motif breaks and no higher-energy isomer has this motif. Although, the isomers (1) and (2) apparently look similar, the position of the exterior Al is significantly higher above the TiB_5 framework in the latter and the distance from Ti atom is also 50 pm longer than the global minimum (1). Analogous global optimization for the cluster of double the size—$Ti_2Al_4B_{12}$ (Supplementary Fig. 13), also reveals the preference for the exposed titanium centers and shows separation of Ti and Al atoms in the clusters with no sign of segregation. These theoretical results on the elementary and double stoichiometries of the cluster agree well with the fairly uniform elemental distribution in the nanopowder as disclosed in the STEM images (Fig. 1).

Binding modes of *exo*-$C_{10}H_{16}$ on $TiAl_2B_6$ cluster

The first step of the interaction between the hydrocarbon *exo*-$C_{10}H_{16}$ with the $TiAl_2B_6$ cluster is the adsorption of the substrate on the catalyst surface. Notice that, for alkanes on cluster catalysts, it is rather typical to not exhibit a physisorbed well on the free energy surface while proceeding directly to chemisorption[64]. Such binding complexes involving the most stable $TiAl_2B_6$ isomer (1) are also simulated, yielding nine lowest energy geometries, which are further Boltzmann-weighted at 750 K (Fig. 5). The global minimum (A) of the resulting $TiAl_2B_6$ - *exo*-$C_{10}H_{16}$ represents 58 % of the total population at 750 K, where the methylene (-CH_2-) bridged C_7H_{10} moiety of the hydrocarbon gets symmetrically docked to the Ti-center of the cluster via the formation of four C-H-Ti linkages. Apparently, the single atom-like structure of the Ti in the cluster catalyst represents a perfect geometrical match with the structure of *exo*-$C_{10}H_{16}$ allowing for simultaneous activation of multiple (3, 4, or even 5) C-H bonds in a single molecule. Due to the binding, the partial positive charge of the Ti center has been noted to decrease from 0.651 to 0.033 (Fig. 6)—suggesting the acceptance of electron density from participating C-H bonds. The average H-Ti distance is calculated to be 210 ± 9 pm which is much shorter than the H-Ti bond length in the physisorbed hydrogen (H_2) on pure Ti-clusters (280 pm)[65]; this suggests a strong activation of the Ti center by the neighboring Al and B atoms. Two five- (C-H-Ti-H-C) and two six-membered (C-C-H-Ti-H-C) cyclic rings evolved during the binding assures enhanced stability in the ensemble (A). In all the lowest energy local minima (B-I), *exo*-$C_{10}H_{16}$ is attached consistently to the Ti center, but the binding motif of the hydrocarbon differs, for example, in the first local minima (B), the cyclic five-membered moiety (C_5H_8) of *exo*-$C_{10}H_{16}$ is bound to Ti—forming five C-H-Ti linkages.

Reaction mechanism of *exo*-$C_{10}H_{16}$ decomposition

The reaction mechanism (Fig. 7) for the catalytic decomposition of *exo*-$C_{10}H_{16}$ generating five-membered hydrocarbon products (Fig. 3) are computed by extending the electronic structure theory calculation involving the lowest energy $TiAl_2B_6$ - *exo*-$C_{10}H_{16}$ binding complex. The entropy-corrected relative free energies at 750 K of the intermediates and transition states (**TS**, Supplementary Fig. 15) with respect to the separated reactants (**R**) have been plotted to generate the free energy profile. The corresponding potential energy surface (PES) at 0 K (Supplementary Fig. 14) suggests the initial adsorbed complex **i1** to be bound by 117 kJ mol^{-1}; however, the complexation being entropically unfavorable, the **i1** energy rises to 53 kJ mol^{-1} at 750 K, which is eventually surmountable at this elevated temperature. From **i1**, the reaction bifurcates into two possible paths—both indicate a Ti-mediated H-

https://doi.org/10.1038/s41467-025-62112-2

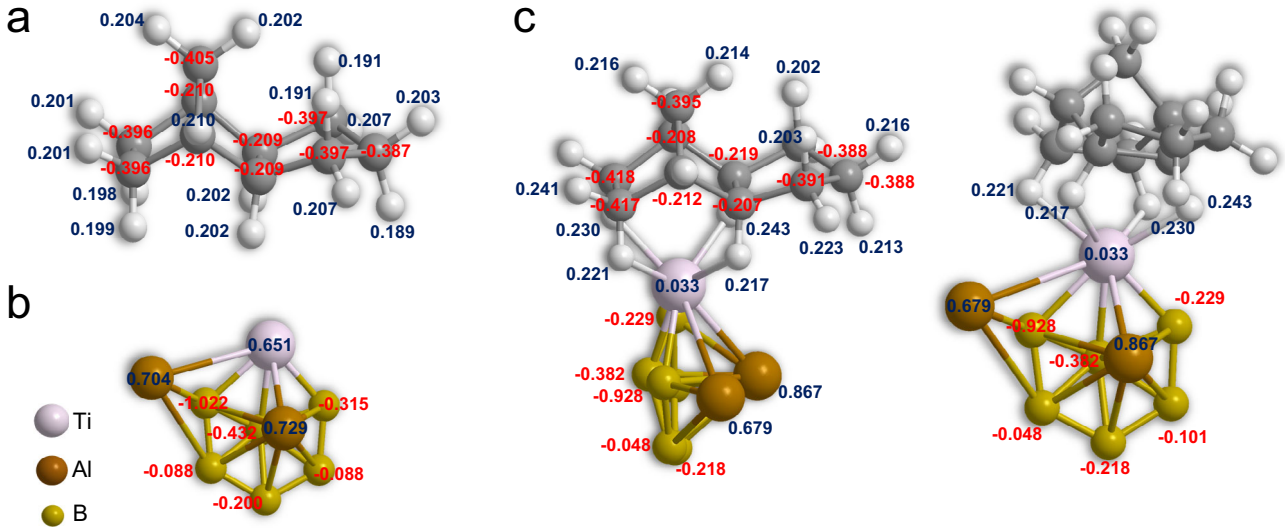

Fig. 6 | Charge distribution on the model cluster and changes due to complex formation. Natural population analysis (NPA) charges (positive charge: *blue*, negative charge: *red*) on the global minima of **a** *exo*-$C_{10}H_{16}$, **b** $TiAl_2B_6$ and the **c** binding complex between *exo*-$C_{10}H_{16}$ and $TiAl_2B_6$ cluster.

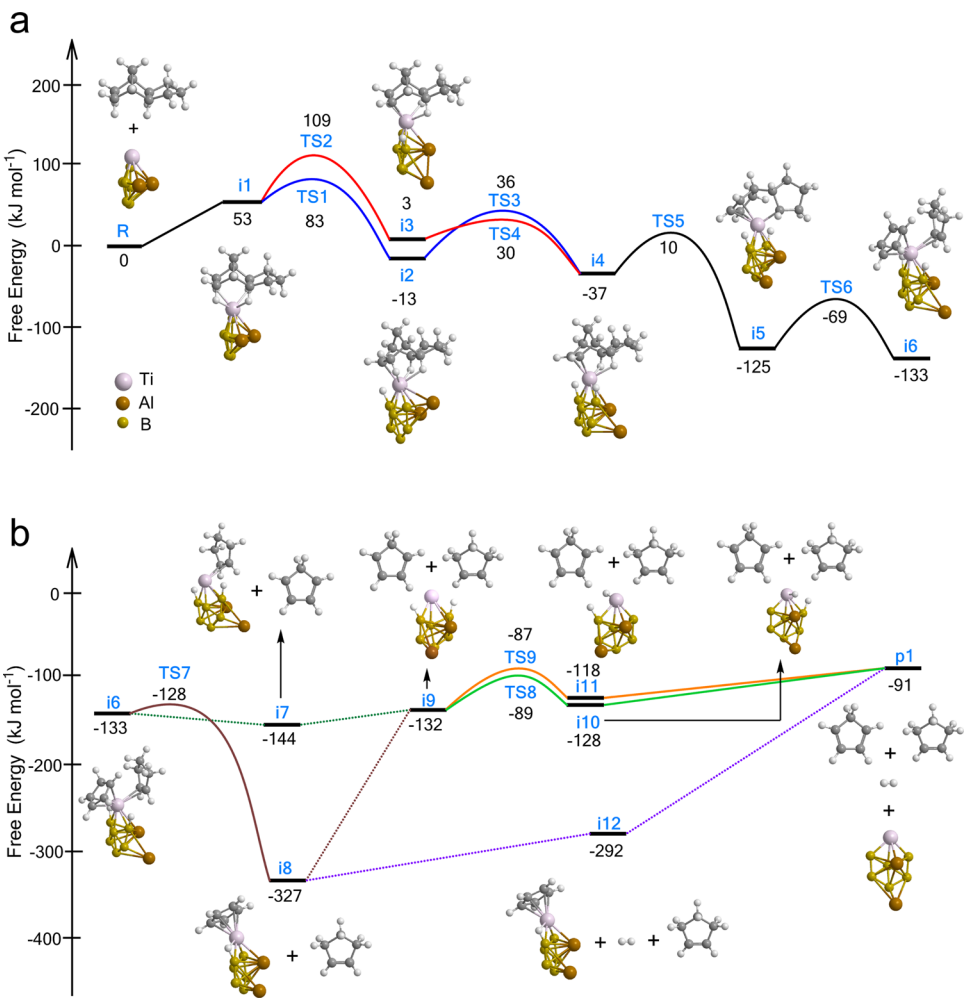

Fig. 7 | Free energy profile of the catalytic cycle at 750 K. Entropy-corrected free energies of the intermediates (**i**) and transition states (**TS**) in the catalytic decomposition of *exo*-$C_{10}H_{16}$ on the global minimum structure of $TiAl_2B_6$ cluster (structure 1 in Fig. 5) at 750 K. The geometries of the **TS**'s are represented in Supplementary Fig. 15. The catalytic steps include - **a** C-H and C-C activations of *exo*-$C_{10}H_{16}$ and **b** desorption of the products from the $TiAl_2B_6$ cluster. The dotted connections are uphill on the enthalpic potential energy surfaces and show no **TS**, while some of them get strongly stabilized by entropy and appear significantly downhill (such as **i6** → **i7**) in the free energy surface; the associated entropic barriers are not computed as they are not expected to alter the reaction kinetics.

https://doi.org/10.1038/s41467-025-62112-2

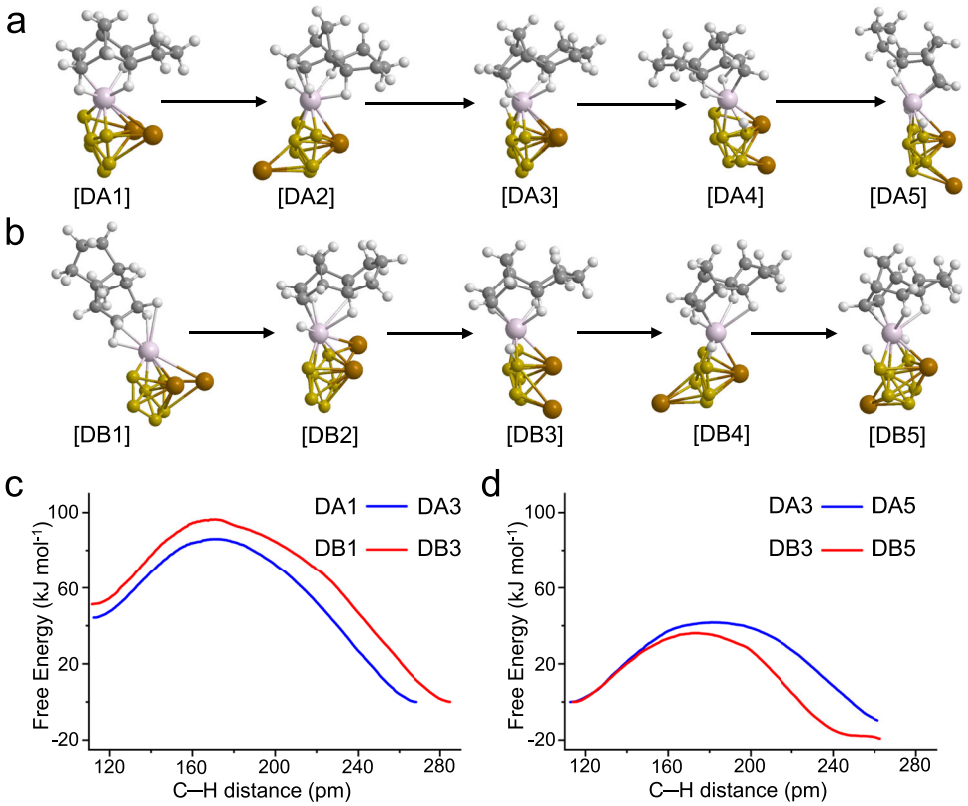

Fig. 8 | Ab initio molecular dynamics (AIMD) simulation of the dehydrogenation steps. AIMD simulation adopting the slow-growth approach for the first H-transfer via the **a** distal side (Supplementary Movies 1, 2) and **b** the proximal side (Supplementary Movies 3, 4) of exterior Al-atom to the *ortho*-B center (DA1 → DA3 and DB1 → DB3, respecectively), followed by the second H-transfer in the alternate directions (DA3 → DA5 and DB3 → DB5, respecectively). Free energy profiles for the **c** first and **d** second H-transfer steps are relative to the respective intermediates (DA3 and DB3) bearing single H-transferred cluster ($HTiAl_2B_6$) bound to $C_{10}H_{15}$. The *blue* and *red* lines represent the free energy profiles for trajectories along path (**a**) and (**b**), respectively.

atom transfer to either of the adjacent B-centers (*ortho* position). In the first path, **i1** → **i2** proceeds via a barrier of 30 kJ mol^{-1} (**TS1**) accompanied by the H-atom transfer to the *ortho*-B atom residing in the opposite (distal) side of the exterior Al atom, whereas the second possible path (**i1** → **i3**) evolves with a higher energy barrier of 56 kJ mol^{-1} (**TS2**), and the H-atom is transferred to the *ortho*-B atom connected to the exterior Al atom (on the proximal side). The **i1** → **i2/i3** steps represent the pivotal first dehydrogenation step and the corresponding transition state energies of 83 and 109 kJ mol^{-1} also represent the maxima in the free energy surface. Each of the intermediates **i2** and **i3** can be portrayed as the binding complex of $C_{10}H_{15}$…$HTiAl_2B_6$, where the remaining hydrocarbon is docked via the Ti center.

Next, **i2** and **i3** undergo a subsequent H-atom shift to the *ortho*-B centers of the cluster—one on the exterior Al side and the other opposite to that, respectively, forming $C_{10}H_{14}$…$H_2TiAl_2B_6$ (**i4**), hence completing the dehydrogenation of the hydrocarbon. The **i4** intermediate also consists of newly formed, direct Ti-C chemical bonds at the expense of two abstracted H-atoms. The respective energy barriers for **i2/i3** → **i4** are 49 and 27 kJ mol^{-1}. Further investigating these initial dehydrogenation steps via ab initio molecular dynamics (AIMD) simulation with the slow-growth approach simultaneously incrementing the reactive C-H length and decrementing the resulting B-H length reveals that the exterior Al-atom is highly fluxional (Fig. 8) during the H-transfer stages to the $TiAl_2B_6$ cluster (Supplementary Movies 1-4). Both of the sequential H-transfers are performed to the Ti-adjacent B-centers consistent with the free energy profile as shown in Fig. 7. DA2 and DB2 represent the free energy maxima of the first H-transfer steps along the sides distal and proximal to the exterior Al-atom, respectively, while DA4 and DB4 are the free energy maxima for the second H-transfer steps. The AIMD simulation visits ensembles of states unlike the discrete path of the NEB method, as it samples accessible configurations of the system over time. For example, our simulation shows a binding mode (DB1) of the hydrocarbon with the model cluster for the first H-transfer proximal to the exterior-Al side that essentially depicts one of the low-lying local minima during complexation (Fig. 5). The energy barriers (42 and 45 kJ mol^{-1}) for the first H-transfer steps are quite similar for both paths (i.e., proximal and distal to the exterior Al-atom), while the second H-transfer step is much favored for the latter (42 versus 36 kJ mol^{-1}), in agreement on the relative preference of paths with the thermodynamic results. It is also noted that in the first step of dehydrogenation via both directions, the interior Al-atom maintains a typical distance of ~250 pm from the B-center that receives the H-atom, and the exterior Al-atom fluctuates across the B-cluster framework, which remains relatively stationary coordinated to Ti (Supplementary Fig. 17). Interestingly, the Al-atoms eventually switch their positions in the second step of the dehydrogenation stabilizing the bound complex.

On the free energy profile of Fig. 7, as we move from **i4** there occurs a ring opening via β-scission in the -C_7H_8 cycle of the hydrocarbon, followed by a twist of the existing five carbon (C5) cyclic ring about the C-C bond which connects the newly formed C5 ring thus generating **i5**. The corresponding transition state (**TS5**) possesses an energy barrier of 47 kJ mol^{-1}. The transformation from **i5** → **i6** depicts the cleavage of ring-connecting C-C bond resulting in two distinct C5 cyclic rings, individually attached to the $H_2TiAl_2B_6$ cluster. The intermediate **i6** denotes the evolution of the experimentally detected cyclic C5 species in the chemisorbed state on the cluster and the steps from

i1 to **i6** collectively demonstrate the efficient catalytic C-H and C-C bond activations by the model TiAlB cluster.

The product desorption into the gas phase and catalyst regeneration steps are shown in Fig. 7b continuing from **i6**. In the **i6** → **i7** step, 1,3-cyclopentadiene (c-C_5H_6) gets desorbed, while the cyclic-C_5H_8 remains attached to the $H_2TiAl_2B_6$ cluster. This step is enthalpically uphill and reaches a plateau for dissociated fragments (Supplementary Fig. 16), but becomes exergonic by 11 kJ mol^{-1}, with the inclusion of entropy (note that the entropically-induced barrier, if any, is not calculated, since the procedure is error-prone, while the barrier would be kinetically inconsequential). On the flipside, highly exergonic desorption (194 kJ mol^{-1}) of cyclopentene (c-C_5H_8) occurs via circumventing a low barrier of only 5 kJ mol^{-1} along **i6** → **i8** step. Upon reaching **i7** and **i8**, collectively, both the decomposed C5 products are released in the gas phase. The intermediates **i7** and **i8** then connect to **i9** via the desorption of remaining c-C_5H_8 and c-C_5H_6, respectively. Both processes are strongly uphill and show no **TS** on the enthalpic PESs (Supplementary Fig. 16) but get somewhat stabilized by entropy (entropic barriers are not calculated). The **i8** → **i9** step is highly endergonic (195 kJ mol^{-1}) as compared to **i7** → **i9** step (12 kJ mol^{-1}) and deemed to be less favorable. Through concerted steps, both the primary cyclic, unsaturated C5 products as identified in the experiments are released in the gas phase at **i9**, revealing simultaneous dehydrogenation of the hydrocarbon *exo*-$C_{10}H_{16}$. In the $H_2TiAl_2B_6$ cluster, the H-atoms remain attached to both of the *ortho*-B atoms (**i9**). However, either of the H-atoms gets transferred to the Ti center by approaching both sides individually through parallel **i9** → **i10** and **i9** → **i11** paths. The H-atoms are mutually placed in the same phase, but above and below the TiB_6 motif in **i10** and **i11**, respectively. Afterwards, **i10** and **i11** merge to **p1** yielding the native $TiAl_2B_6$ cluster and hydrogen (H_2) liberated in the gas phase, the latter is also identified experimentally. The endergonic desorption (also uphill enthalpically without a **TS**) of molecular hydrogen (**i8** → **i12**, 35 kJ mol^{-1}) can also occur prior to that of cyclopentadiene (c-C_5H_6); the latter undergoes a highly endergonic desorption (**i12** → **p1**, 201 kJ mol^{-1}) generating the $TiAl_2B_6$ cluster. Comparing the energetics of **i7**/**i8** → **p1** steps, it can be noted that the desorption of C5 hydrocarbons preferably occurs prior to the molecular hydrogen desorption, evident from the low endoergicity of ~30 kJ mol^{-1} for **i10**/**i11** → **p1** step compared to that of **i12** → **p1** path. Overall, the **i1** to **p1** steps depict the complete catalytic cycle of the model cluster and demonstrate dehydrogenation followed by a typical [4 + 2] retro-Diels-Alder reaction of the hydrocarbon *exo*-$C_{10}H_{16}$.

Computationally, the effect of temperature can be very precisely evaluated by comparing the free energy profiles at 0 K (Supplementary Fig. 14) and 750 K (Fig. 7), where the initial step (**R** → **i1**) is energetically favored at low temperatures (−117 kJ mol^{-1}); on the contrary, represents an entropically unfavorable barrier (53 kJ mol^{-1}) with the rise in temperature to 750 K. However, at 0 K, the desorption steps from the catalyst (**i6** → **P1**) reveal high endoergicity (451 kJ mol^{-1}), but lowered to only 42 kJ mol^{-1} at the elevated temperature of 750 K. Overall, the reaction from (**R** → **P1**) is unfavorable (endergonic by 176 kJ mol^{-1}) at 0 K, and eventually turns out to be spontaneous with an exoergicity of −91 kJ mol^{-1} at 750 K, corroborating the critical thermocatalytic property of TiAlB nanopowder. The enhanced yield of cyclopentadiene (c-C_5H_6) with the rise in temperature demonstrates that the desorption from the $TiAl_2B_6$ cluster becomes energetically much favorable (**i6** → **p1**) and abstraction of an additional H-atom from c-C_5H_6 to the model cluster is much likely to occur leading to the formation of cyclopentadienyl (C_5H_5) radical, exclusively at high temperature (1050 K).

It is evident from the abovementioned computational findings that the lone Ti atom acts as the pivotal docking center of the TiAlB model cluster, where the approaching hydrocarbon gets anchored efficiently via the formation of multiple Ti−hydrogen interactions. This multitude of binding interactions is facilitated by the large size of Ti and its high possible coordination number ranging up to eight[66,67]. Later in the free energy surface, Ti also forms direct Ti-C bonds to hold the hydrocarbon fragments. This phenomenon is well recognized in the case of alkene polymerization by Ti-containing Ziegler−Natta catalysts, where the active catalyst undergoes Ti-C bond formation with the inserted hydrocarbon during initiation and propagation steps of the polymerization; however, the Ti-center in Ziegler-Natta happens to be significantly more electropositive compared to that of the present catalyst system[68].

The B_n clusters have been proven to be an exclusive class of inorganic ligands utilized as building blocks in material science and chemistry[62]. Similarly, here the B_6 framework can be identified as the host of the entire cluster structure. Besides, it also serves as the hydrogen storage entity through stepwise H-atom transfer from *exo*-$C_{10}H_{16}$—a property previously noticed for B clusters[68,69].

Finally, the Al atoms hold the structural integrity of the cluster via large electron donation to the B cluster strengthening the electrostatic interaction[70,71]. The position of Al on the cluster is apparently fluxional as evident from both NEB and AIMD simulations, indicating little coordination preference and purely an electrostatic coordination to the B. The position of Al is changing throughout the reaction profile, making space for stored H-atoms produced through dehydrogenation. While Al acts as a stabilizing agent for the cluster, it appears to be mechanistically important, in that it does not coordinate to the cluster in a too specific a manner. It is possible that the fluxionality effect is particularly pronounced in the small cluster model and would be more modest in larger NPs. Thus, all components of the TiAlB cluster (and, by inference, NPs) appear to play a role in efficient *exo*-$C_{10}H_{16}$ decomposition: Ti is the single atom active site, B is the hydrogen storage unit, and Al is a catalyst stabilizer that yet makes space for the reaction when needed. Extrapolation of the computational picture to the bulk indicates that the catalysis occurs at the surface of the material where exposed Ti and its adjacent exposed B (i.e., *ortho*-B) centers are directly involved in the elementary C-H and C-C bond breaking processes of the hydrocarbon.

Through the combined investigation of the molecular beam emitting from the chemical microreactor by in situ, isomer-selective, synchrotron single-photon ionization mass spectrometry and extensive electronic structure theory calculation, the immense catalytic potential of the sonochemically-generated amorphous TiAlB NP towards low temperature decomposition of a saturated hydrocarbon has been revealed. The theoretical treatment elucidates an initial formation of binding complex between *exo*-$C_{10}H_{16}$ and $TiAl_2B_6$ model cluster through docking of the hydrocarbon onto the Ti atom followed by two successive hydrogen shifts from the $C_{10}H_{16}$ molecule to the B cluster atoms yielding a $C_{10}H_{14}$ moiety chemically bound to the Ti. The hydrocarbon moiety then ring-opens via two consecutive carbon-carbon bond cleavages in two steps ([4 + 2] retro-Diels-Alder reaction) to dehydrogenated products as 1,3-cyclopentadiene (c-C_5H_6) and cyclopentene (c-C_5H_8)—both of them are identified in the gas phase experimentally. The recombination of the two H-atoms on the cluster and release of molecular hydrogen into the gas-phase completes the catalytic cycle.

This study demonstrates that Ti, which is otherwise insensitive to C-H activation in its metallic state, in this case is a key participant in the catalytic C-H activation when bound to readily available light elements: B and Al, which all participate in the catalytic activation process. The initial C-H bond cleavages prior to the retro Diels-Alder reaction results into dehydrogenation, ultimately releasing molecular hydrogen as detected experimentally, while lowering the barrier of first C-H bond cleavage to only 83–109 kJ mol^{-1} compared to that of the homolytic cleavage of pure *exo*-$C_{10}H_{16}$ being ~400 kJ mol^{-1}. This multi-metal catalyst consists of terrestrially abundant elements, thus making it potentially an inexpensive

alternative to Pt and other noble metal catalysts. Clearly, additional experimental and computational studies are required to expand the aforementioned conclusions drawn from the present work. The immense potential for low temperature C-H activation capabilities of the mixed-metal, sonochemically-generated TiAlB nanopowder, cannot be understated and subsequent work exploring catalytic conversions of the light alkanes involving C-H bond cleavage as the primary step—such as dehydrogenation of propane, ethane and functionalizing methane—further yielding high value chemicals are to be explored in imminent future. These projected studies are the very first steps toward a comprehensive understanding of the low temperature catalytic activity of the TiAlB NP, further exploring the effects of the surface structure and elemental composition on the onset of the decomposition, catalytic activation, and product spectrum.

Methods

Experimental

Synthesis of titanium aluminum boron nanopowder. First, in a dinitrogen (N_2) atmosphere glovebox, $TiCl_4$ (10 g, 52.7 mmol) was added to a standard 500 mL Schlenk flask and charged with 350 mL of Et_2O. Separately, in a custom 1 L pearshaped reactor with a built-in condenser and a side arm-equipped with a ChemGlass Teflon-valve (size 20), $LiBH_4$ (3.5 g, 160.6 mmol) and $LiAlH_4$ (2 g, 52.7 mmol) were dissolved in 250 mL of Et_2O. The reactor containing the $LiBH_4$/$LiAlH_4$ solution was connected to a Schlenk line and placed in a benchtop sonicator bath and the $TiCl_4$ solution was transferred by cannula into the sonicating solution of $LiAlH_4$ and $LiBH_4$. Immediately upon addition, a black precipitate was formed, releasing large amounts of heat and gas. This gas evolution acted to slow the rate of addition by cannula, ensuring that the reaction did not run away. The reaction was allowed to sonicate overnight (18 h) with the solution reaching reflux temperatures, and the reactor was constantly purged with N_2. After stopping sonication and cooling to room temperature, the reaction vessel was brought into a N_2 glovebox and the reaction was gravity filtered through a fine porosity-fitted glass funnel. The raw products were processed by heating *in vacuo* at 100 °C overnight. After cooling, the samples were washed with THF to remove leftover salts and dried at room temperature under a dynamic vacuum[45].

Solid state NMR and Raman spectroscopy. Solid-state nuclear magnetic resonance (NMR) spectroscopy was performed on an Agilent NMR500 spectrometer using a 4-mm HXY triple resonance NMR probe. The ^{27}Al resonance frequency was 130.32 MHz, and the ^{11}B resonance frequency was 160.48 MHz. All spectra were obtained under a dry N_2 atmosphere at 30 °C. Spectra were analyzed in Matlab. Raman spectra were collected with a Renishaw inVia Raman microscope instrument equipped with a diode pumped solid state laser (532 nm—green) with 2 cm^{-1} spectral resolution. Typical data acquisition time was 120 s per scan with 50× objective and 5 accumulations for averaging. The laser energy was maintained at only 25 mW to avoid any destruction of the sample.

Details of the catalytic microreactor. The nascent gas phase products formed in the thermal decomposition of helium-seeded *exo*-tetrahydrodicyclopentadiene (*exo*-$C_{10}H_{16}$) vapor through the titanium-aluminum-boron nanopowder (TiAlB NP) packing at distinct temperatures from 300 K to 1050 K through the chemical microreactor[46–49] (Supplementary Fig. 5) are detected in situ by using single photon VUV photoionization (PI) mass spectrometry[49]. The experiments were carried out at the Chemical Dynamics Beamline (9.0.2.) installed in Advanced Light Source (ALS).

Briefly, the microreactor was a resistively heated silicon carbide (SiC) tube of 20 mm length and 1 mm inner diameter, which was tightly packed with TiAlB NP about a length of 10 mm inside the SiC tube. The packing was done in such a way that the interaction and residence time of the hydrocarbon with the nanoparticle surface is enough to trace the reactivity. A gas mixture at a pressure of 500 Torr with *exo*-$C_{10}H_{16}$ (TCI America; 94%) in helium carrier gas (He; Airgas; 99.999%) was prepared by bubbling helium gas through *exo*-$C_{10}H_{16}$ kept in a stainless-steel bubbler at 300 K. The gas mixture was introduced into the silicon carbide tube where the temperature can reach up to 1600 ± 20 K as monitored by type-C thermocouple. After exiting the reactor, the molecular beam containing the pyrolysis products, passed a skimmer and entered a detection chamber, which housed the Wiley-McLaren Re-TOF-MS. The products were photoionized in the extraction region of the spectrometer by exploiting synchrotron quasi-continuous tunable VUV light from the Chemical Dynamics Beamline 9.0.2 and detected with a microchannel plate detector. Compared to hard electron impact ionization, soft VUV-PI has the unique advantage of an ideally fragment-free ionization of the neutrals. Further, by tuning the VUV energy, structural isomers can be identified.

Here, mass spectra were recorded in 0.05 eV intervals from 8.00 eV to 11.50 eV. A set of additional mass spectra was also measured at 15.4 eV to determine hydrogen and methane yields having ionization energies of 15.4 eV and 12.6 eV, respectively, which cannot be ionized below 11.5 eV. The PIE curves, which report the intensity of a single mass-to-charge ratio (m/z) versus the photon energy, were extracted by integrating the signal collected at a specific m/z selected for the species of interest over the range of photon energies in 0.05 eV increments and normalized to the incident photon flux. The PIE curves were then fit with a linear combination of known PIE curves to isomer-selectively identify the products.

For each experimental run, the TiAlB catalyst in the microreactor was warmed up to a well-defined temperature (the maximum being 1050 K) and upon equilibration of the temperature, mass spectra were recorded averaged over 5 million scans each which was equivalent to about 30 min of scan time. Upon completion of the data acquisition, it was cooled down to 293 K with pure helium flow through the reactor tube (without seeded *exo*-$C_{10}H_{16}$). This process was repeated to acquire the next set of mass spectra, i.e., a total of five sets of heating-cooling cycles. The experimental approach mentioned via the repetitive heating-cooling-heating cycle of the catalyst packing not only ensures the reproducibility, but also carefully inspects the catalyst performance over time and a broad range of temperature.

Computational

The structure of *exo*-$C_{10}H_{16}$ was geometrically optimized using Density Functional Theory with Orca 5.0.4[72]. BLYP functional[73,74] was used with the def2-TZVP basis set[75] and def2/J auxiliary basis set[76]. D3BJ was the method for the correction of dispersion forces[77,78]. The structure of TiAlB NP was determined using stochastic structure search. Specifically, the PGOPT protocol was used for structure generation using the BLDA algorithm[79], and over 700 unique structures of the chemical formula: $TiAl_2B_6$ were produced. Geometry optimization was done using HF-3c, and refined using BLYP functional with def2-TVZP and def2/J basis sets. D3BJ was used to correct for dispersion forces. Each minimum was confirmed with vibrational frequency analysis. For the resulting $TiAl_2B_6$ cluster geometries, the Boltzmann population at 750 K was calculated.

Binding of the $TiAl_2B_6$ cluster with the hydrocarbon *exo*-$C_{10}H_{16}$ was also simulated using the obtained lowest energy $TiAl_2B_6$ isomers. The orientation of *exo*-$C_{10}H_{16}$ when docked to each of these lowest energy $TiAl_2B_6$ isomers was randomly sampled, and the geometries of the complexes were optimized using BLYP functional with def2-TVZP and def2/J basis sets. D3BJ was used to correct for dispersion forces. The resulting $TiAl_2B_6$ - *exo*-$C_{10}H_{16}$ ensembles were again Boltzmann-weighted at 750 K. The lowest energy binding complex represents 58% of the population at 750 K.

Finally, the energetics of the reaction depicted in Fig. 7 were calculated starting from the lowest energy $TiAl_2B_6$ - *exo*-$C_{10}H_{16}$ binding complex, using the nudged elastic band (NEB) method[80,81]. The transition states were confirmed by having a single imaginary frequency aligned with the reaction coordinate. All reactants, intermediates, and products were confirmed to have no imaginary frequencies. When calculating free energies, the entropy of the $TiAl_2B_6$ cluster was accounted for differently than the entropy of gaseous species. The $TiAl_2B_6$ cluster is treated differently since it is a placeholder for the TiAlB nanoparticle, which should have no translational and rotational entropy. The entropy corrections of gaseous species were calculated using ideal gas statistical mechanics as implemented in Orca 5.0.4. This includes translational entropy based on the Sackur-Tetrode equation[82], vibrational entropy using the quasi-RRHO method[83], and rotational entropy computed according to Herzberg[84]. Entropy corrections for all chemical species containing the $TiAl_2B_6$ cluster consisted of only the vibrational entropy calculated using the quasi-RRHO method.

To assess the dynamics of the cluster during dehydrogenation, AIMD were performed in CP2K[85] using the BLYP[73,74] functional and D3BJ dispersion correction[77,78] with TZVP-MOLOPT-SR-GTH basis set and GTH pseudopotentials[86,87] along with a Nose-Hoover Thermostat[88] set at 750 K. Intermediates from the free energy profile were placed in a 25 Å × 25 Å × 25 Å unit cell and pulled along the reaction coordinate by constraints. Starting from **i2** and proceeding toward **i1** and **i4**, the reactive C-H bond length and formed B-H bond length were incremented or decremented accordingly by 0.0001 Å/fs to arrive at the same bond lengths as in **i1** and **i4**. Similarly, the C-H and B-H distances were incremented or decremented by 0.0001 Å/fs from **i3** to approach the bond lengths found in **i1** and **i5**. The slow-growth approach[89] was utilized to determine the free energy difference between two states, 0 and 1, by integrating the constraining force over the reaction coordinate ξ:

$$\Delta F = \int_{\xi(0)}^{\xi(1)} \left(\frac{\partial F}{\partial \xi}\right) \cdot d\xi \quad (1)$$

Data availability

Data generated or analyzed during this study are included in the main text and Supplementary Information. Source data are provided with this paper. Molecular dynamics (AIMD) simulation results have been deposited in the Zenodo repository under accession code https://doi.org/10.5281/zenodo.15764927. All data are available from the corresponding authors upon request. Source data are provided with this paper.

References

1. Döbereiner, J. W. Newly discovered remarkable properties of the suboxides of platinum, of oxidized platinum sulfide, and of metallic platinum dust. *Ann. Phys.***72**, 193–198 (1822).
2. Marei, M. N. et al. Comparative study of the catalytic oxidation of hydrocarbons on platinum and palladium wires and nanoparticles. *Energy Fuels* **36**, 2044–2057 (2022).
3. Periana, R. A. et al. Platinum catalysts for the high-yield oxidation of methane to a methanol derivative. *Science* **280**, 560–564 (1998).
4. Hiam, L., Wise, H. & Chaikin, S. Catalytic oxidation of hydrocarbons on platinum. *J. Catal.* **10**, 272–276 (1968).
5. Cheng, N. et al. Platinum single-atom and cluster catalysis of the hydrogen evolution reaction. *Nat. Commun.* **7**, 13638 (2016).
6. Rylander, P. N. in *Catalytic Hydrogenation Over Platinum Metals* (ed Paul N. Rylander) 81–120 (Academic Press, 1967).
7. Sinfelt, J. H. Catalysis—Science and Technology: *Catalytic Reforming of Hydrocarbons* Vol. 1, 257–300 (De Gruyter, 1982).
8. Keshavarz, M. H., Monjezi, K. H., Esmailpour, K. & Zamani, M. Performance assessment of some isomers of saturated polycyclic hydrocarbons for use as jet fuels. *Propellants Explos. Pyrotech.* **40**, 309–314 (2015).
9. Carter, J. H. et al. Direct and oxidative dehydrogenation of propane: from catalyst design to industrial application. *Green. Chem.* **23**, 9747–9799 (2021).
10. Chen, S. et al. Propane dehydrogenation: catalyst development, new chemistry, and emerging technologies. *Chem. Soc. Rev.* **50**, 3315–3354 (2021).
11. Trimm, D. L. & Doerr, L. A. The catalytic oxidation of propylene to benzene. *J. Catal.* **26**, 1–10 (1972).
12. Xue, X.-S., Ji, P., Zhou, B. & Cheng, J.-P. The essential role of bond energetics in C–H activation/functionalization. *Chem. Rev.* **117**, 8622–8648 (2017).
13. Labinger, J. A. & Bercaw, J. E. Understanding and exploiting C–H bond activation. *Nature* **417**, 507–514 (2002).
14. Shilov, A. E. & Shul'pin, G. B. Activation of C–H bonds by metal complexes. *Chem. Rev.* **97**, 2879–2932 (1997).
15. Zhu, H. & Ziegler, T. Probing the influence of trans and leaving ligands on the ability of square-planar platinum(II) complexes to activate methane. A theoretical study. *Organometallics* **28**, 2773–2777 (2009).
16. Nave, S., Tiwari, A. K. & Jackson, B. Dissociative chemisorption of methane on Ni and Pt surfaces: mode-specific chemistry and the effects of lattice motion. *J. Phys. Chem. A* **118**, 9615–9631 (2014).
17. Lebrilla, C. B. & Maier, W. F. Carbon-hydrogen bond activation on platinum. A mechanistic study. *J. Am. Chem. Soc.* **108**, 1606–1616 (1986).
18. Labinger, J. A. Platinum-Catalyzed C–H Functionalization. *Chem. Rev.* **117**, 8483–8496 (2017).
19. Wang, Y., Hu, P., Yang, J., Zhu, Y.-A. & Chen, D. C–H bond activation in light alkanes: a theoretical perspective. *Chem. Soc. Rev.* **50**, 4299–4358 (2021).
20. Somorjai, G. A. & Blakely, D. W. Mechanism of catalysis of hydrocarbon reactions by platinum surfaces. *Nature* **258**, 580–583 (1975).
21. Chang, X., Lu, Z., Wang, X., Zhao, Z.-J. & Gong, J. Tracking C–H bond activation for propane dehydrogenation over transition metal catalysts: work function shines. *Chem. Sci.* **14**, 6414–6419 (2023).
22. Marcinkowski, M. D. et al. Pt/Cu single-atom alloys as coke-resistant catalysts for efficient C–H activation. *Nat. Chem.* **10**, 325–332 (2018).
23. Nakaya, Y., Hirayama, J., Yamazoe, S., Shimizu, K. -i & Furukawa, S. Single-atom Pt in intermetallics as an ultrastable and selective catalyst for propane dehydrogenation. *Nat. Commun.* **11**, 2838 (2020).
24. Wu, Z. et al. Changes in catalytic and adsorptive properties of 2 nm Pt3Mn nanoparticles by subsurface atoms. *J. Am. Chem. Soc.* **140**, 14870–14877 (2018).
25. Sun, G., Fuller, J. T. III, Alexandrova, A. N. & Sautet, P. Global activity search uncovers reaction induced concomitant catalyst restructuring for alkane dissociation on model Pt catalysts. *ACS Catal.* **11**, 1877–1885 (2021).
26. Cesar, L. G. et al. Identification of a Pt3Co Surface intermetallic alloy in Pt–Co propane dehydrogenation catalysts. *ACS Catal.* **9**, 5231–5244 (2019).
27. Searles, K. et al. Highly productive propane dehydrogenation catalyst using silica-supported Ga–Pt nanoparticles generated from single-sites. *J. Am. Chem. Soc.* **140**, 11674–11679 (2018).
28. Sun, G. et al. Breaking the scaling relationship via thermally stable Pt/Cu single atom alloys for catalytic dehydrogenation. *Nat. Commun.* **9**, 4454 (2018).
29. Cai, W. et al. Subsurface catalysis-mediated selectivity of dehydrogenation reaction. *Sci. Adv.* **4**, eaar5418 (2018).
30. Cybulskis, V. J. et al. Zinc promotion of platinum for catalytic light alkane dehydrogenation: Insights into geometric and electronic effects. *ACS Catal.* **7**, 4173–4181 (2017).

31. Albarède, F. *Geochemistry: An Introduction* 5–24 (Cambridge University Press, 2009).
32. Ghosh, P. C. High platinum cost: obstacle or blessing for commercialization of low-temperature fuel cell technologies. *Clean. Technol. Environ. Policy* **19**, 595–601 (2017).
33. Billeter, E., Łodziana, Z. & Borgschulte, A. Surface properties of the hydrogen–titanium system. *J. Phys. Chem. C.* **125**, 25339–25349 (2021).
34. Sun, Q., Wang, Q., Jena, P. & Kawazoe, Y. Clustering of Ti on a C60 surface and its effect on hydrogen storage. *J. Am. Chem. Soc.* **127**, 14582–14583 (2005).
35. Cremaschi, P. & Whitten, J. L. Chemisorption of hydrogen on titanium: embedding theory and comparisons with small clusters. *Surf. Sci.* **112**, 343–358 (1981).
36. Chaudhuri, S. & Muckerman, J. T. First-Principles Study of Ti-catalyzed hydrogen chemisorption on an Al surface: A critical first step for reversible hydrogen storage in NaAlH4. *J. Phys. Chem. B* **109**, 6952–6957 (2005).
37. Wang, J. W. & Gong, H. R. Adsorption and diffusion of hydrogen on Ti, Al, and TiAl surfaces. *Int. J. Hydrog. Energy* **39**, 6068–6075 (2014).
38. Dong, H., Hou, T., Lee, S.-T. & Li, Y. New Ti-decorated B40 fullerene as a promising hydrogen storage material. *Sci. Rep.* **5**, 9952 (2015).
39. Huo, Y. et al. Boron-doping effect on the enhanced hydrogen storage of titanium-decorated porous graphene: a first-principles study. *Int. J. Hydrog. Energy* **46**, 40301–40311 (2021).
40. Gandeepan, P. et al. 3d Transition metals for C–H activation. *Chem. Rev.* **119**, 2192–2452 (2019).
41. Ramírez-de-Arellano, J. M., Carrillo, I. & Magaña, L. F. Chemisorption of carbon monoxide, carbon dioxide and "methanephobia" on the [0001] titanium surface. *Appl. Surf. Sci.* **478**, 128–133 (2019).
42. Epshteyn, A., Yonke, B. L., Miller, J. B., Rivera-Díaz, J. L. & Purdy, A. P. Sonochemically generated air-stable bimetallic nanopowders of group 4 transition metals with aluminum. *Chem. Mater.* **25**, 818–824 (2013).
43. Huba, Z. J., Donakowski, M. D. & Epshteyn, A. Gram-scale, low temperature, sonochemical synthesis of stable amorphous Ti–B powders containing hydrogen. *Chem. Mater.* **29**, 1467–1471 (2017).
44. Epshteyn, A., Weismiller, M. R., Huba, Z. J., Maling, E. L. & Chaimowitz, A. S. Optimization of a high-energy Ti–Al–B nanopowder. *Fuel. Energy Fuels* **31**, 1811–1819 (2017).
45. Finn, M. T., Chaloux, B. L. & Epshteyn, A. Exploring the effects of reaction conditions on morphology and stability of sonochemically generated Ti–Al–B fuel powders. *Energy Fuels* **34**, 11373–11380 (2020).
46. Biswas, S. et al. Counterintuitive catalytic reactivity of the aluminum oxide "passivation" shell of aluminum nanoparticles facilitating the thermal decomposition of exo-tetrahydrodicyclopentadiene (JP-10). *J. Phys. Chem. Lett.* **14**, 9341–9350 (2023).
47. Biswas, S. et al. Efficient oxidative decomposition of jet-fuel exo-tetrahydrodicyclopentadiene (JP-10) by aluminum nanoparticles in a catalytic microreactor: An online vacuum ultraviolet photoionization study. *J. Phys. Chem. A* **128**, 1665–1684 (2024).
48. Biswas, S. et al. Stress-alteration enhancement of the reactivity of aluminum nanoparticles in the catalytic decomposition of exo-tetrahydrodicyclopentadiene (JP-10). *J. Phys. Chem. A* **128**, 3613–3624 (2024).
49. Zhao, L. et al. A vacuum ultraviolet photoionization study on high-temperature decomposition of JP-10 (exo-tetrahydrodicyclopentadiene). *Phys. Chem. Chem. Phys.* **19**, 15780–15807 (2017).
50. Tarasov, V. P. & Kirakosyan, G. A. Aluminohydrides: Structures, NMR, solid-state reactions. *Russ. J. Inorg. Chem.* **53**, 2048–2081 (2008).
51. Xu, S. et al. High-field one-dimensional and two-dimensional 27Al magic-angle spinning nuclear magnetic resonance study of θ-, δ-, and γ-Al2O3 dominated aluminum oxides: toward understanding the Al sites in γ-Al2O3. *ACS Omega* **6**, 4090–4099 (2021).
52. Ammar, A. et al. Investigation of the electronic and structural properties of potassium hexaboride, KB6, by transport, magnetic susceptibility, EPR, and NMR measurements, temperature-dependent crystal structure determination, and electronic band structure calculations. *Inorg. Chem.* **43**, 4974–4987 (2004).
53. Huynh, W., Taylor, J. W., Harman, W. H. & Conley, M. P. Solid-state 11B NMR studies of coinage metal complexes containing a phosphine substituted diboraanthracene ligand. *Dalton Trans.* **50**, 14855–14863 (2021).
54. MacKenzie, K. J. D., Smith, M. E., Kemp, T. F. & Voll, D. Crystalline aluminium borates with the mullite structure: A 11B and 27Al solid-state NMR study. *Appl. Magn. Reson.* **32**, 647–662 (2007).
55. Jensen, J. O. Vibrational frequencies and structural determination of aluminum tetrahydroborate. *Spectrochim. Acta A Mol. Biomol. Spectrosc.* **59**, 1565–1578 (2003).
56. Wang, S. et al. Study on the infrared and Raman spectra of Ti3AlB2, Zr3AlB2, Hf3AlB2, and Ta3AlB2 by first-principles calculations. *Sci. Rep.* **14**, 15030 (2024).
57. Wdowik, U. D., Twardowska, A. & Rajchel, B. Vibrational spectroscopy of binary titanium borides: first-principles and experimental studies. *Adv. condens. Matter Phys.* **2017**, 4207301 (2017).
58. Ekoi, E. J., Gowen, A., Dorrepaal, R. & Dowling, D. P. Characterisation of titanium oxide layers using Raman spectroscopy and optical profilometry: Influence of oxide properties. *Results Phys.* **12**, 1574–1585 (2019).
59. Photonionization Cross Section Database (Version 2.0); National Synchrotron Radiation Laboratory; Hefei, China, http://flame.nsrl.ustc.edu.cn/database/
60. Lai, Y. et al. Low-temperature oxidation of methane on rutile TiO2(110): identifying the role of surface oxygen species. *JACS Au* **4**, 1396–1404 (2024).
61. Brotton, S. J. et al. Combined spectroscopic and computational investigation on the oxidation of exo-tetrahydrodicyclopentadiene (JP-10; C10H16) doped with titanium–aluminum–boron reactive metal nanopowder. *J. Phys. Chem. A* **126**, 125–144 (2022).
62. Alexandrova, A. N., Boldyrev, A. I., Zhai, H.-J. & Wang, L.-S. All-boron aromatic clusters as potential new inorganic ligands and building blocks in chemistry. *Coord. Chem. Rev.* **250**, 2811–2866 (2006).
63. Alexandrova, A. N. et al. Structure and bonding in B6- and B6: planarity and antiaromaticity. *J. Phys. Chem. A* **107**, 1359–1369 (2003).
64. Guo, H., Sautet, P. & Alexandrova, A. N. Reagent-triggered isomerization of fluxional cluster catalyst via dynamic coupling. *J. Phys. Chem. Lett.* **11**, 3089–3094 (2020).
65. Guo, J. X. et al. First-principles calculations of hydrogen molecule adsorption on Ti (0001)-(2×1) surface. *Appl. Surf. Sci.* **255**, 7512–7516 (2009).
66. del Horno, E., Jover, J., Mena, M., Pérez-Redondo, A. & Yélamos, C. Low-valent titanium species stabilized with aluminum/boron hydride fragments. *Chem. Eur. J.* **28**, e202103085 (2022).
67. Huang, L.-F., Grabowski, B., McEniry, E., Trinkle, D. R. & Neugebauer, J. Importance of coordination number and bond length in titanium revealed by electronic structure investigations. *Phys. Status Solidi B* **252**, 1907–1924 (2015).
68. Sinn, H. & Kaminsky, W. in *Advances in Organometallic Chemistry* Vol. 18 (eds Stone, F. G. A. & West, R.) 99–149 (Academic Press, 1980).
69. Zhang, Z., Cui, Z.-H., Jimenez-Izal, E., Sautet, P. & Alexandrova, A. N. Hydrogen evolution on restructured B-rich WB: metastable surface states and isolated active sites. *ACS Catal.* **10**, 13867–13877 (2020).

70. Romanescu, C., Sergeeva, A. P., Li, W.-L., Boldyrev, A. I. & Wang, L.-S. Planarization of B7− and B12− clusters by isoelectronic substitution: AlB6− and AlB11−. *J. Am. Chem. Soc.* **133**, 8646–8653 (2011).
71. Huynh, M. T. & Alexandrova, A. N. Persistent covalency and planarity in the BnAl6–n2− and LiBnAl6–n− (n = 0–6) cluster ions. *J. Phys. Chem. Lett.* **2**, 2046–2051 (2011).
72. Neese, F. The ORCA program system. *Wiley Interdiscip. Rev. Comput. Mol. Sci.* **2**, 73–78 (2012).
73. Lee, C., Yang, W. & Parr, R. G. Development of the Colle-Salvetti correlation-energy formula into a functional of the electron density. *Phys. Rev. B* **37**, 785–789 (1988).
74. Becke, A. D. Density-functional exchange-energy approximation with correct asymptotic behavior. *Phys. Rev. A* **38**, 3098–3100 (1988).
75. Weigend, F. & Ahlrichs, R. Balanced basis sets of split valence, triple zeta valence and quadruple zeta valence quality for H to Rn: design and assessment of accuracy. *Phys. Chem. Chem. Phys.* **7**, 3297–3305 (2005).
76. Weigend, F. Accurate Coulomb-fitting basis sets for H to Rn. *Phys. Chem. Chem. Phys.* **8**, 1057–1065 (2006).
77. Grimme, S., Ehrlich, S. & Goerigk, L. Effect of the damping function in dispersion corrected density functional theory. *J. Comput. Chem.* **32**, 1456–1465 (2011).
78. Grimme, S., Antony, J., Ehrlich, S. & Krieg, H. A consistent and accurate ab initio parametrization of density functional dispersion correction (DFT-D) for the 94 elements H-Pu. *J. Chem. Phys.* **132**, 154104 (2010).
79. Zhai, H., Ha, M.-A. & Alexandrova, A. N. AFFCK: adaptive force-field-assisted ab initio coalescence kick method for global minimum search. *J. Chem. Theory Comput.* **11**, 2385–2393 (2015).
80. Henkelman, G. & Jónsson, H. Improved tangent estimate in the nudged elastic band method for finding minimum energy paths and saddle points. *J. Chem. Phys.* **113**, 9978–9985 (2000).
81. Henkelman, G., Uberuaga, B. P. & Jónsson, H. A climbing image nudged elastic band method for finding saddle points and minimum energy paths. *J. Chem. Phys.* **113**, 9901–9904 (2000).
82. Grimus, W. 100th anniversary of the Sackur–Tetrode equation. *Ann. Phys.***525**, A32–A35 (2013).
83. Grimme, S. Supramolecular binding thermodynamics by dispersion-corrected density functional theory. *Chem. Eur. J.* **18**, 9955–9964 (2012).
84. Herzberg, G. & Crawford, B. L. Jr. Infrared and Raman spectra of polyatomic molecules. *J. Phys. Chem.* **50**, 288–288 (1946).
85. Kühne, T. D. et al. CP2K: An electronic structure and molecular dynamics software package - Quickstep: Efficient and accurate electronic structure calculations. *J. Chem. Phys.* **152**, 194103 (2020).
86. Krack, M. Pseudopotentials for H to Kr optimized for gradient-corrected exchange-correlation functionals. *Theor. Chem. Acc.* **114**, 145–152 (2005).
87. Goedecker, S., Teter, M. & Hutter, J. Separable dual-space Gaussian pseudopotentials. *Phys. Rev. B* **54**, 1703–1710 (1996).
88. Nosé, S. A unified formulation of the constant temperature molecular dynamics methods. *J. Chem. Phys.* **81**, 511–519 (1984).
89. Woo, T. K., Margl, P. M., Blöchl, P. E. & Ziegler, T. A combined car–parrinello QM/MM implementation for ab initio molecular dynamics simulations of extended systems: application to transition metal catalysis. *J. Phys. Chem. B* **101**, 7877–7880 (1997).

Acknowledgements

The Hawaii group was supported by the United States Office of Naval Research (ONR) under Contract Number N00014-22-1-2010. UCLA research was sponsored by Air Force Office of Scientific Research grant AFOSR FA9550-22-1-0381. This work used computational and storage services associated with the DOD HPC, National Energy Research Scientific Computing Center, which is supported by the Office of Science of the U.S. Department of Energy under Contract No. DE-AC02-05CH11231, and UCLA IDRE Shared Cluster Hoffman2. M.A. & N.D. are supported by the Director, Office of Science, Office of Basic Energy Sciences, of the U.S. Department of Energy under Contract No. DE-AC02-05CH11231, through the Gas Phase Chemical Physics program of the Chemical Sciences Division.

Author contributions

S.B., R.I.K., and M.A. conceptualized the experiment, M.F. and A.E. synthesized the material, B.M.H., C.A.K., and P.M.G. characterized the material, S.B. and N.D. performed the catalysis experiment at beamline, S.B. and D.P. analyzed the experimental data, J.C. and W.G. performed the computations and analyzed the data, H.W.T.M. mentored J.C. and analyzed the computational data, S.B. wrote the original draft of the manuscript, S.B., R.I.K., M.A., A.N.A., M.F., and A.E. revised the draft of the manuscript with the input from all the authors.

Competing interests

The authors declare no competing interests.

Additional information

Supplementary information The online version contains supplementary material available at https://doi.org/10.1038/s41467-025-62112-2.

Correspondence and requests for materials should be addressed to Albert Epshteyn, Anastassia N. Alexandrova, Musahid Ahmed or Ralf I. Kaiser.

Peer review information *Nature Communications* thanks Guido Kickelbick, Luis Fernando Magaña and the other, anonymous, reviewer(s) for their contribution to the peer review of this work. A peer review file is available.